

Inference-Time Refinement Closes the Synthetic-Real Gap in Tabular Diffusion

Eugenio Lomurno^{*†1}, Filippo Balzarini^{†1}, Francesco Benelle^{†1}, Francesca Pia Panaccione^{†1}, and Matteo Matteucci¹

¹Politecnico di Milano, AIRLab, Italy

Abstract

Diffusion-based generators set the current state of the art for synthetic tabular data, deployed downstream wherever direct access to real records is restricted. These methods approach but rarely exceed real-data utility on downstream tasks, and closing this synthetic–real performance gap has so far been pursued exclusively at training time, via architectural advances, scaling, and retraining of monolithic generators. The inference-time alternative, i.e., refining the outputs of a pre-trained backbone with parameters left untouched, has remained largely unexplored for tabular synthesis. We introduce **TARDIS** (Tabular generation through Refinement, Distillation, and Inference-time Sampling), an inference-time refinement framework that operates on a frozen pre-trained backbone, configured per dataset by a Tree-structured Parzen Estimator search over score-level guidance during reverse diffusion, with each trial’s objective set by an inner grid search over post-hoc sample selectors and an optional soft-label distillation step. The search space encodes a single mathematical pattern we name *Bidirectional Chamfer Refinement* (BCR): the symmetric Chamfer functional between synthetic and real samples is minimized both continuously, via a score-level gradient during reverse diffusion, and discretely, via batch-ranking post-generation. On the majority of datasets the search selects BCR-aligned configurations over alternatives encoded in the search space, evidence both for BCR as the dominant refinement pattern and for TARDIS’s per-dataset search as a procedure that recovers this pattern. Across 15 binary, multiclass, and regression benchmarks TARDIS achieves a median +8.6% downstream-task improvement over models trained on real data (95% CI [+3.3, +16.4], Wilcoxon $p = 0.016$, 11/15 strict wins) and improves over the underlying TabDiff backbone on all 15 datasets (mean +12.9%, $p < 10^{-4}$), matching the backbone on manifold fidelity, diversity, and sample-level privacy. The synthetic–real gap is therefore not primarily a training-time problem: on the studied corpus, inference-time refinement of a pre-trained tabular diffusion backbone reaches and exceeds real-data utility in 1 to 80 minutes on a single consumer-grade GPU.

Keywords: Tabular Diffusion · Inference-Time Refinement · Chamfer Guidance · Synthetic Data

1 Introduction

Mixed-type tabular records remain the dominant input format of applied machine learning. When direct access to such records is restricted, synthetic generation enables downstream training [7, 9], and diffusion-based generators currently set the state of the art [22]. Despite steady architectural progress, downstream learners trained on the output of these generators approach but rarely match the utility of equivalent learners trained on real data, leaving a persistent *synthetic–real gap*.

Existing approaches to closing this gap follow a single paradigm: improve the generator. Each new architecture, e.g., TabDiff [20] with its per-feature noise schedules, adds complexity but yields only marginal gains on the headline downstream metric, leaving real-data utility unmatched on most standard benchmarks. The implicit assumption underlying this trajectory is that the gap must be closed at training time, with the generator as the only target of intervention.

An alternative paradigm has emerged in image synthesis, where inference-time guidance methods modify the sampling process of a pre-trained diffusion model at no addi-

tional training cost. Classifier-free guidance [11] steers sampling toward class-conditional or prompt-conditional outputs by interpolating score predictions; Chamfer Guidance [6] steers it toward arbitrary user-specified reference batches by perturbing the score with the gradient of a bidirectional Chamfer functional. Direct transfer of this paradigm to tabular synthesis is non-trivial, however, due to (i) mixed-type feature spaces that lack a canonical differentiable distance, (ii) the absence of a standardized representation space analogous to CLIP for images, and (iii) the dual fidelity-utility objective specific to the train-on-synthetic-test-on-real (TSTR) setting.

At its core, our approach generates many candidate samples from the pre-trained backbone and retains those that best match the real-data manifold, both by steering generation toward it and by filtering the output pool afterward. We call this framework **TARDIS** (Tabular generation through Refinement, Distillation, and Inference-time Sampling), an inference-time refinement framework that operates on a frozen pre-trained tabular diffusion backbone. TARDIS is grounded in the *Bidirectional Chamfer Refinement* (BCR) principle: a continuous score-level perturbation during reverse diffusion and a discrete post-generation subsampling step both minimize the same symmetric Chamfer functional between candidates and

* Corresponding author: eugenio.lomurno@polimi.it

† These authors contributed equally to this work.

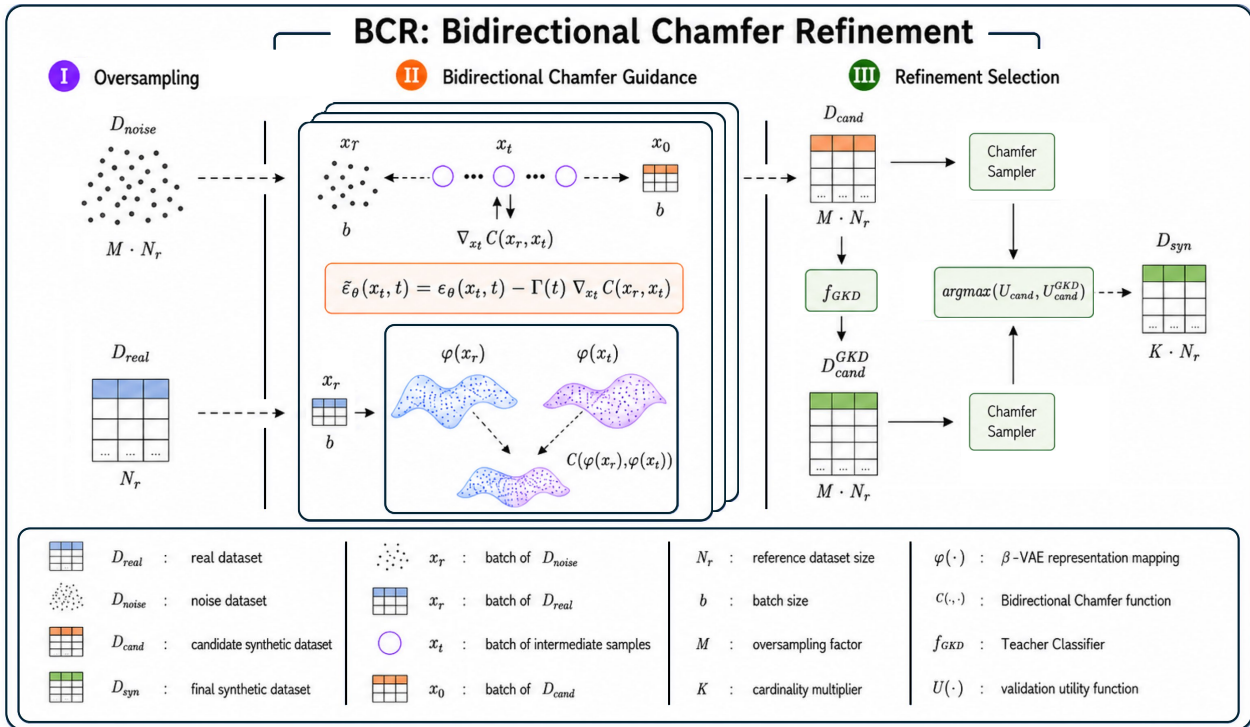


Figure 1: TARDIS pipeline. Stage I draws an oversampled noise pool D_{noise} of cardinality $M \cdot N_r$ from the latent space \mathcal{Z} . Stage II denoises D_{noise} via reverse diffusion, perturbing the score $\varepsilon_\theta(x_t, t)$ with the gradient of the bidirectional Chamfer functional C between the current candidate batch x_t and a real reference batch x_r , projected through a representation map φ ; this produces the candidate pool D_{cand} . Stage III selects D_{syn} of cardinality $K \cdot N_r$ from D_{cand} via a Chamfer Sampler, optionally preceded by Generative Knowledge Distillation f_{GKD} that relabels candidates with soft targets; the final variant is chosen by argmax over the validation utility U . The figure illustrates the BCR-headline configuration with β -VAE mapping and Chamfer Sampler. The full TARDIS framework generalizes Stage II to also support disabled-guidance and identity-mapping variants, and Stage III to a grid over five samplers (Section 3.3, Appendix D).

a real reference batch, with the continuous step concentrating probability mass near the real-data manifold and the discrete step pruning residual off-manifold candidates. BCR addresses the three obstacles above in unified form: it handles (i) and (ii) through a representation map φ instantiated per dataset either as the identity on z -score-normalized features or as the encoder of a tabular β -VAE, providing a differentiable representation that absorbs mixed-type heterogeneity without requiring a canonical metric; and (iii) by balancing fidelity (synthetic-to-real) and coverage (real-to-synthetic) terms in a single bidirectional functional, coupling the TSTR utility objective directly to manifold-distance minimization.

The framework operationalizes BCR through three stages (Figure 1): Stage I oversamples a noise pool, Stage II applies the score-level Chamfer perturbation during reverse diffusion, and Stage III ranks the resulting candidate pool under the same functional, optionally after a soft-label distillation step [10, 19]. Stage II hyperparameters are tuned per dataset by a Tree-structured Parzen Estimator search [1]; at each trial Stage III runs a grid over selectors and the distillation toggle, returning its best validation utility as the trial’s objective.

Empirically, across 15 heterogeneous tabular benchmarks (binary classification, multiclass classification, regression), TARDIS surpasses real-data utility on 11 of 15 datasets at a median +8.6% improvement on the headline downstream metric, improves over the underlying

TabDiff backbone on all 15, and matches the backbone on manifold fidelity, diversity, and sample-level privacy. The synthetic–real gap is therefore, on this corpus, an inference-time rather than a training-time problem.

TARDIS is, to the best of our knowledge, the first inference-time refinement framework for tabular diffusion; BCR is the unifying principle coupling its continuous and discrete steps under a single Chamfer functional; and our empirical results show that inference-time refinement suffices to close the synthetic–real gap without retraining.

2 Related Work

We review prior work along three axes that intersect in TARDIS, i.e., tabular generative modelling, inference-time guidance for diffusion, and post-hoc curation of generated samples.

Tabular generative models. Existing approaches treat the synthetic–real utility gap as a problem of the generator architecture. GAN-based methods, e.g., CTGAN [24] and CTAB-GAN+ [26], address mixed-type generation through conditional sampling and mode-specific normalization; VAE and autoregressive families, with TVAE [24] and TabularARGN [21], factorize the joint via variational decoders or per-feature autoregressive heads; diffusion-based formulations, with TabDDPM [15], STaSy [13], CoDi [17], TabSyn [25], and TabDiff [20], set the current state of the art through increasingly elaborate score-based and latent-

space designs. Each step advances the architecture, but none operates on the output distribution of an already-trained backbone. TARDIS departs from this trajectory by refining that output distribution at inference time, with the backbone left frozen.

Inference-time guidance for diffusion. Inference-time guidance steers a pre-trained diffusion model toward task-specific or user-specified outputs without retraining. Building on standard score-based diffusion [12], classifier-free guidance [11] interpolates between conditional and unconditional score predictions for class- and prompt-conditional image synthesis; Chamfer Guidance [6] extends this to reference-based steering by perturbing the score with the gradient of a bidirectional Chamfer functional between candidates and a reference set in image space. Tabular counterparts are absent in the literature. TARDIS adapts the Chamfer construction to the tabular setting through a representation map φ instantiated per dataset (identity on z -score-normalized features or the encoder of a β -VAE), and adds a discrete post-hoc selection stage that Chamfer Guidance does not include, unifying both levels under the same functional.

Synthetic-data filtering and post-hoc refinement. Post-hoc curation of generated samples emerged in image synthesis with the Chamfer Sampler of [6], which ranks an oversampled candidate pool by bidirectional manifold proximity to a real reference set. In tabular synthesis the closest precedent is ISSOSYNTH [8], which oversamples a pre-trained generator and selects a subset minimizing a binned L_1 distance over low-order marginals via discrete iterative-proportional-fitting. Soft-label distillation has been used in tabular and image synthesis to inject teacher knowledge into synthetic training sets [10, 18]; feature-space oversampling for class imbalance, e.g., SMOTE [4], operates without a learned metric or generative pool. TARDIS reframes the oversample-and-select pattern of ISSOSYNTH as one of two coupled operational levels, pairing the discrete selection step with continuous score-level guidance during reverse diffusion, replacing binned-marginal distances with a continuous metric in φ -space, and unifying both levels under a single Chamfer functional.

Across these three clusters, no prior work occupies the intersection TARDIS targets: *post-pretraining* refinement of a tabular diffusion backbone, with continuous and discrete steps unified under a single Chamfer functional. The closest precedents are Chamfer Guidance [6] in the image domain (continuous guidance only) and ISSOSYNTH [8] in tabular synthesis (discrete selection only); TARDIS combines and extends both.

3 Methodology

We introduce **TARDIS** (Tabular generation through Refinement, Distillation, and Inference-time Sampling), a three-stage inference-time refinement framework operating on a frozen pre-trained tabular diffusion backbone $G_\theta : \mathcal{Z} \rightarrow \mathcal{X} \times \mathcal{Y}$, where \mathcal{Z} is the latent noise space, $\mathcal{X} = \mathcal{X}_{\text{num}} \times \mathcal{X}_{\text{cat}}$ the mixed-type feature space, and \mathcal{Y} the target space (\mathbb{R} for regression, finite for classification).

Given a real dataset $D_{\text{real}} \subset \mathcal{X} \times \mathcal{Y}$ of cardinality N_r and a held-out test set D_{test} , TARDIS produces a synthetic dataset D_{syn} of cardinality $K \cdot N_r$ targeting the train-on-synthetic-test-on-real (TSTR) utility

$$\mathcal{U}_{\text{syn}} = \psi(A(D_{\text{syn}}), D_{\text{test}}), \quad (1)$$

$$\mathcal{U}_{\text{real}} = \psi(A(D_{\text{real}}), D_{\text{test}}), \quad (2)$$

where A is a downstream learner and ψ a task-appropriate metric (AUROC, RMSE). The synthetic-real gap is the empirical regularity $\mathcal{U}_{\text{syn}} < \mathcal{U}_{\text{real}}$ across mainstream tabular generators; TARDIS aims to close, and where possible reverse, this gap at inference time.

The framework comprises three stages (Figure 1). Stage I draws an oversampled noise pool $D_{\text{noise}} \subset \mathcal{Z}$ of cardinality $M \cdot N_r$. Stage II denoises D_{noise} through the reverse-diffusion process of G_θ , optionally perturbing the predicted score at each step with the gradient of a bidirectional Chamfer functional against D_{real} , yielding the candidate pool D_{cand} of cardinality $M \cdot N_r$. Stage III selects D_{syn} from D_{cand} via post-hoc batch ranking under the same functional, optionally preceded by a soft-label distillation step. Stages II and III thus minimize the same Chamfer functional \mathcal{C} at two complementary operational levels: continuously, via score-level gradient descent during sampling, and discretely, via batch ranking after sampling. We refer to this joint minimization as *Bidirectional Chamfer Refinement* (BCR). Stage II hyperparameters are tuned per dataset by a Tree-structured Parzen Estimator (TPE) search [1]; at each trial, Stage III performs an inner grid search over its selector and distillation toggle, and the maximum validation utility across that grid is returned as the trial’s objective.

3.1 Stage I: Oversampling

Stage I draws $M \cdot N_r$ samples from the latent prior of \mathcal{Z} , forming the noise pool D_{noise} . The oversampling factor M controls the redundancy available to Stage III: each retained sample is selected from M/K candidates. We fix $M = 50$ across all benchmarks. BCR requires $M > K$ so that the Stage III refinement operates on a non-trivial selection set; the saturation of utility as $K \rightarrow M$ is characterized in Appendix A.

3.2 Stage II: Bidirectional Chamfer Guidance

Stage II denoises D_{noise} through the reverse-diffusion process of G_θ . During reverse diffusion the predicted score is optionally perturbed by the gradient of a bidirectional Chamfer functional against D_{real} , steering candidates toward the real-data manifold. The resulting candidate pool D_{cand} has cardinality $M \cdot N_r$. The TPE search introduced above selects all Stage II hyperparameters jointly per dataset; the full search space is reported in Appendix F, Table 5.

Bidirectional Chamfer functional. Let $\varphi : \mathcal{X} \rightarrow \mathbb{R}^d$, with $d \in \mathbb{N}^+$, be a representation map and $A, B \subset \mathcal{X}$ two finite sample sets. We adopt the symmetric Chamfer

functional [6],

$$\mathcal{C}(A, B) = \frac{1}{|A|} \sum_{a \in A} \min_{b \in B} \|\varphi(a) - \varphi(b)\|_2 + \frac{1}{|B|} \sum_{b \in B} \min_{a \in A} \|\varphi(a) - \varphi(b)\|_2, \quad (3)$$

which decomposes into a fidelity term penalizing deviations from A to its nearest match in B (first sum) and a coverage term penalizing the symmetric direction (second sum). \mathcal{C} is symmetric, non-negative, and zero if and only if $\varphi(A) = \varphi(B)$ as multisets (Appendix A).

Guidance variants. The TPE search exposes guidance as a binary toggle. When disabled, the score perturbation of Equation 5 is dropped and Stage II reduces to standard reverse diffusion. When enabled, the representation map φ admits two mutually exclusive forms, also exposed to the TPE search: (i) *identity mapping*, with φ the identity on z -score-normalized features and the Chamfer gradient computed in the data space; (ii) *β -VAE mapping*, with φ the encoder of a tabular β -VAE [2, 14] learned per dataset on D_{real} and the Chamfer gradient computed in its latent space. Figure 1 illustrates the β -VAE-mapping variant.

β -VAE encoder. The encoder is trained on D_{real} under the standard β -VAE evidence lower bound,

$$\mathcal{L}_{\text{VAE}}(x) = \mathcal{L}_{\text{rec}}(x, \hat{x}) + \beta(t) \cdot D_{\text{KL}}(q_\varphi(z | x) \| p(z)), \quad (4)$$

with prior $p(z) = \mathcal{N}(0, I)$, KL annealing $\beta(t)$ from one of five schedule families, and a composite reconstruction loss combining mean squared error on numerical features with cross-entropy on categorical groups, averaged within group to balance the gradient contribution across feature types. The latent dimension $d \in \{4, 8, 16, 32\}$ is selected by the TPE search; full schedule families and training hyperparameters are deferred to Appendix C.

Score perturbation. At each guidance step t , the perturbed score is

$$\tilde{\varepsilon}_\theta(x_t, t) = \varepsilon_\theta(x_t, t) - \Gamma(t) \cdot \nabla_{x_t} \mathcal{C}(x_t, x_r), \quad (5)$$

where ε_θ is the score predicted by the backbone, $\Gamma(t) \geq 0$ a time-dependent scaling factor, and $x_r \subset D_{\text{real}}$ a reference batch sampled at the start of each generation and held fixed across diffusion steps. Guidance is applied at t_g steps of the reverse trajectory rather than at every step, with t_g tuned per dataset (Table 5); the remaining steps use the unperturbed score ε_θ . Equation 5 is an approximation: unlike classifier-free guidance [11], it does not correspond to exact posterior sampling under a likelihood defined by \mathcal{C} , and $\Gamma(t)$ keeps the perturbation small relative to ε_θ , acting as a soft steering signal. The schedule $\Gamma(t)$ is selected from four families (constant, linear, cosine, sine) bounded by $\gamma_{\min}, \gamma_{\max}$; the reference batch x_r is either class-conditional or global.

3.3 Stage III: Refinement Selection

Stage III selects D_{syn} of cardinality $K \cdot N_r$ from the candidate pool D_{cand} produced by Stage II. The selection is performed by an inner grid search over a binary Generative Knowledge Distillation (GKD) toggle and five sampler

variants (10 combinations); for each TPE trial of Stage II, the configuration maximizing validation utility is retained, and the resulting maximum is returned to the outer search as that trial’s objective.

Chamfer Sampler. The Chamfer Sampler is the discrete counterpart of the Stage II score perturbation: it minimizes the same functional \mathcal{C} of Equation 3, evaluated at the pair (B_k, D_{real}) , by post-hoc batch ranking rather than gradient descent. Partitioning D_{cand} into batches $\{B_k\}_{k=1}^{M \cdot N_r / b}$ of size b ,

$$\mathcal{C}(B_k, D_{\text{real}}) = \underbrace{\frac{1}{|B_k|} \sum_{x \in B_k} \min_{r \in D_{\text{real}}} \|\varphi(x) - \varphi(r)\|_2}_{m_{\text{sr}}(B_k): \text{fidelity}} + \underbrace{\frac{1}{|D_{\text{real}}|} \sum_{r \in D_{\text{real}}} \min_{x \in B_k} \|\varphi(x) - \varphi(r)\|_2}_{m_{\text{rs}}(B_k): \text{coverage}}, \quad (6)$$

batches are ranked ascending by $\mathcal{C}(B_k, D_{\text{real}})$ and the top-ranked union of $K \cdot N_r$ samples constitutes D_{syn} . The representation map φ is inherited from Stage II when guidance is enabled, and defaults to the identity mapping when guidance is disabled.

Equation 6 and Equation 5 jointly minimize the same Chamfer functional \mathcal{C} on the same representation space φ at two complementary operational levels: continuous gradient descent during reverse diffusion (Stage II) concentrates probability mass near the real-data manifold; discrete batch ranking after diffusion (Stage III) prunes off-manifold residuals. This joint minimization is the BCR principle; a saturation argument for the M/K ratio is given in Appendix A.

Alternative samplers. The grid search additionally exposes four alternative samplers (Stratified, IBOSS [23], HDBSCAN [3], MDSampler), which differ from the Chamfer Sampler in their selection criterion: feature-space stratification, information-theoretic boundary coverage, density-based clustering, and one-directional manifold-distance ranking. Their inclusion enables the grid to recover single-stage variants when Stage II disables guidance, in which case the Chamfer functional’s bidirectional structure is no longer matched by Stage II and a one-directional alternative may suffice. Full definitions and pseudocode are deferred to Appendix D.

Generative Knowledge Distillation. GKD [10, 19] replaces the hard targets in D_{cand} with soft-label distributions produced by a teacher classifier f_{GKD} trained on D_{real} , yielding the relabeled candidate set $D_{\text{cand}}^{\text{GKD}}$; features are left unchanged (Appendix E). GKD is structurally undefined for continuous regression targets and is restricted to classification benchmarks. The grid search treats GKD as an orthogonal toggle: each sampler is evaluated on both D_{cand} and $D_{\text{cand}}^{\text{GKD}}$, and the higher-utility variant is retained.

4 Experiments and Results

Datasets and configurations. We evaluate TARDIS on 15 publicly available tabular benchmarks (UCI and Kaggle) spanning binary classification (5 datasets), multiclass classification (4), and regression (6), with structural diversity across feature counts (8 to 46), feature types, instance counts (666 to 53,940), class balance, and domain coverage (healthcare, finance, environment, education, social science). All datasets use a 90/5/5 train/validation/test split seeded identically across models. The TPE search and inner grid of Section 3 are run independently per dataset; per-dataset structural attributes and the configurations selected by the search are reported in Appendix F (Tables 4 and 6, respectively).

Backbone selection. TabDiff [20] is selected as the backbone via a controlled 1:1 cardinality comparison against TabSyn [25] and TabularARGN [21] on the 10 benchmarks of our corpus shared with prior tabular diffusion work. Aggregating the per-dataset relative deviation from real-data utility on the headline metric, TabDiff is closest to Real with $\Delta\% = -6.7\%$, followed by TabSyn (-8.9%) and TabularARGN (-25.7%). Per-dataset breakdowns and full metric coverage are deferred to Appendix B.

Evaluation protocol. The downstream learner is XGBoost [5] with early stopping on the validation split. We adopt the train-on-synthetic-test-on-real (TSTR) protocol, reporting AUROC for binary classification, weighted-AUROC for multiclass classification, and RMSE for regression as the primary downstream metric ψ . We report the per-dataset relative improvement $\Delta\%$ in ψ both over the real-data baseline (sign-corrected for RMSE) and over the TabDiff backbone, and aggregate it across the 15 datasets via the median with bootstrap 95% confidence intervals; statistical significance is assessed by Wilcoxon signed-rank paired tests, with per-dataset means as the unit of comparison. Fidelity (Precision) and diversity (Recall) are reported via manifold metrics [16]; privacy via Distance to Closest Record (DCR) and Nearest-Neighbor Distance Ratio (NNDR). Per-dataset and per-metric breakdowns are deferred to Appendix G. All experiments run on a single Nvidia GTX 1080 Ti (12 GB, 2017 consumer GPU) with 5 random seeds per configuration.

4.1 Main results

Aggregate downstream utility. Across the 15 benchmarks (Table 1), TARDIS achieves a median $\Delta\%$ improvement of $+8.6$ over $\mathcal{U}_{\text{real}}$ (95% CI $[+3.3, +16.4]$, Wilcoxon $p = 0.016$), with strict positive improvement on 11 of 15 datasets and parity on Diamonds. Against the TabDiff backbone, the improvement is uniform: $\Delta\% > 0$ on every dataset, with median $+6.3$ and mean $+12.9$ (95% CI $[+7.2, +19.2]$, $p < 10^{-4}$). The proximity of mean and median over $\mathcal{U}_{\text{real}}$ (mean $+9.7$ vs. median $+8.6$) indicates a tight distribution of dataset-level gains rather than an aggregate driven by outliers.

Cardinality ablation. Setting $K = 1$ disables the oversample-and-select component of TARDIS, reducing the framework to Stage II guidance applied at the same cardinality as D_{real} . This restricted variant (TARDIS $\times 1$,

Table 1) reaches mean $\Delta\% = +1.4$ over TabDiff but does not significantly improve over $\mathcal{U}_{\text{real}}$ (Wilcoxon $p > 0.05$). The full TARDIS gain therefore depends jointly on the candidate redundancy of Stage I and on the BCR-driven discrete refinement of Stage III; Stage II guidance alone is insufficient to close the synthetic–real gap.

Utility inverse scaling. Per-dataset variance in TARDIS’s $\Delta\%$ over $\mathcal{U}_{\text{real}}$ correlates inversely with the real-data baseline (Figure 2a): the four datasets where the real baseline approaches the metric ceiling (Adult AUROC 0.927, Bank 0.929, Magic 0.956, Diamonds 0.943) yield $\Delta\% \in [-3.0, +0.9]$, with Bank’s -3.0 the only negative point. Beijing represents the analogous case for regression: the target admits a near-linear structure that XGBoost on real data already exploits, leaving a residual deviation of -12.1 . Improvement concentrates instead on datasets where $\mathcal{U}_{\text{real}}$ reflects data scarcity, label noise, or class imbalance: Solar Flare ($+39.5$, 1,066 instances), Diabetic Retinopathy ($+29.5$, 1,151 instances), Student Performance ($+20.9$, 666 instances), News ($+16.7$, imbalanced regression target), Music ($+15.2$, multiclass with rare classes).

4.2 Empirical signatures of BCR

Cardinality saturation. We sweep $K \in \{0.1, 0.5, 1, 3, 5, 10, 20\}$ with $M = 50$ fixed on three benchmarks spanning the $\mathcal{U}_{\text{real}}$ regime: Adult (AUROC 0.927), Diamonds (AUROC 0.943), and Beijing (RMSE 0.033). All three datasets exhibit monotone improvement in ψ (Figure 2b), with knees at $K \approx 3$ on Adult and $K \approx 5$ on Diamonds; on Beijing the curve continues to descend through $K = 20$ without plateauing within the swept range. TARDIS overtakes TabDiff near $K \approx 1.0$ on all three datasets, indicating that BCR refinement begins to add value already at real cardinality. The plateau location is ordered consistently with the strength of $\mathcal{U}_{\text{real}}$: Adult saturates early below Real, Diamonds reaches parity with Real near $K = 20$, and Beijing remains below Real within the swept range.

Sampler-guidance coupling. The TPE search and inner grid expose a structural alignment between Stage II guidance and Stage III sampler choice, recovered without explicit constraint (Table 6). Of the 9 datasets where guidance is enabled, all 9 select the Chamfer Sampler in Stage III; of the 6 datasets where guidance is disabled, 4 (Bank, Magic, Music, Abalone) select the MDSampler, and the remaining 2 (Adult, Solar Flare) select the Chamfer Sampler with GKD enabled (the only configurations with $K \leq 1$, where the candidate pool is too sparse for the MDSampler’s purely fidelity-driven selection to retain coverage). The configurations therefore cluster into two coherent regimes: guided pool with bidirectional Chamfer-based selection (9/15), and unguided pool with one-directional manifold-distance selection (4/15). When Stage II shapes the candidate pool toward the real manifold via $\nabla\mathcal{C}$, the discrete sampler that minimizes the same \mathcal{C} dominates; when Stage II is disabled and $K \gg 1$, the simpler one-directional MDSampler suffices.

Low-cardinality regime. The configuration-level evi-

Table 1: Per-dataset downstream utility under TSTR with XGBoost. Primary metric ψ : AUROC for BC, weighted-AUROC for MC (\uparrow), RMSE for R (\downarrow). $\Delta\%R$ and $\Delta\%T$ are sign-corrected relative changes vs. Real and TabDiff. Best per row in bold; aggregates over the 15 datasets at the bottom.

Dataset	Task	Real	TabDiff	TARDIS \times 1	TARDIS	$\Delta\%R$	$\Delta\%T$
<i>Regression — RMSE \downarrow</i>							
Solar Flare	R	0.1025	0.0923	0.0869	0.0620	+39.5	+32.8
Infrared Therm.	R	0.0541	0.0585	0.0562	0.0482	+10.9	+17.6
Abalone	R	0.081	0.079	0.075	0.074	+8.6	+6.3
Insurance	R	0.118	0.132	0.143	0.110	+6.8	+16.7
Beijing	R	0.033	0.051	0.051	0.037	-12.1	+27.5
News	R	0.01154	0.01194	0.01000	0.00961	+16.7	+19.5
<i>Binary classification — AUROC \uparrow</i>							
Diabetic Retin.	BC	0.6976	0.6671	0.6697	0.9037	+29.5	+35.5
Adult	BC	0.927	0.913	0.922	0.924	-0.3	+1.2
Default	BC	0.764	0.765	0.768	0.775	+1.4	+1.3
Magic	BC	0.956	0.940	0.949	0.965	+0.9	+2.7
Bank	BC	0.929	0.856	0.863	0.901	-3.0	+5.3
<i>Multiclass classification — weighted-AUROC \uparrow</i>							
Student Perf.	MC	0.7392	0.7453	0.6796	0.8939	+20.9	+19.9
Contraceptive	MC	0.6491	0.6838	0.677	0.7077	+9.0	+3.5
Music	MC	0.729	0.823	0.833	0.840	+15.2	+2.1
Diamonds	MC	0.943	0.930	0.934	0.943	0.0	+1.4
<i>Mean</i>						+9.7	+12.9
<i>Median</i>						+8.6	+6.3
<i>95% CI</i>						[+3.3, +16.4]	[+7.2, +19.2]
<i>p (Wilcoxon)</i>						0.016	$< 10^{-4}$
<i>Wins</i>						11/15	15/15

dence in Table 6 surfaces a regime separation along K that we term the *low-cardinality regime* ($K \leq 1$). Across the 15 benchmarks, GKD is enabled on 2 datasets only, both with $K \leq 1$ (Adult $K=0.5$, Solar Flare $K=0.1$); on the remaining 13, all with $K \geq 8.5$, the search disables GKD. The pattern is consistent with the qualitative mechanism: at low K the candidate pool is too sparse for the Chamfer Sampler to recover utility through selection alone, and the soft-label channel becomes the dominant signal; at high K the pool is large enough for selection to suffice, and GKD’s smoothing becomes a net negative. The analysis is restricted to classification, since GKD is structurally undefined for continuous regression targets and is consistently disabled on the 6 regression datasets in the corpus. We position GKD as a regime-specific component for hardware-constrained downstream applications, complementing the main result rather than competing with it.

4.3 Fidelity, diversity, privacy, and runtime

Fidelity and diversity. Manifold Precision (fidelity) and Recall (diversity) [16] are preserved at the TabDiff backbone level on all 15 datasets (Table 2): mean Precision 0.949 (TARDIS) vs. 0.947 (TabDiff), mean Recall 0.995 vs. 0.994, with per-dataset absolute deviations bounded by 0.043 and 0.003 respectively. The BCR-driven refinement does not collapse the synthetic distribution onto a subset of the real manifold, the canonical failure mode of

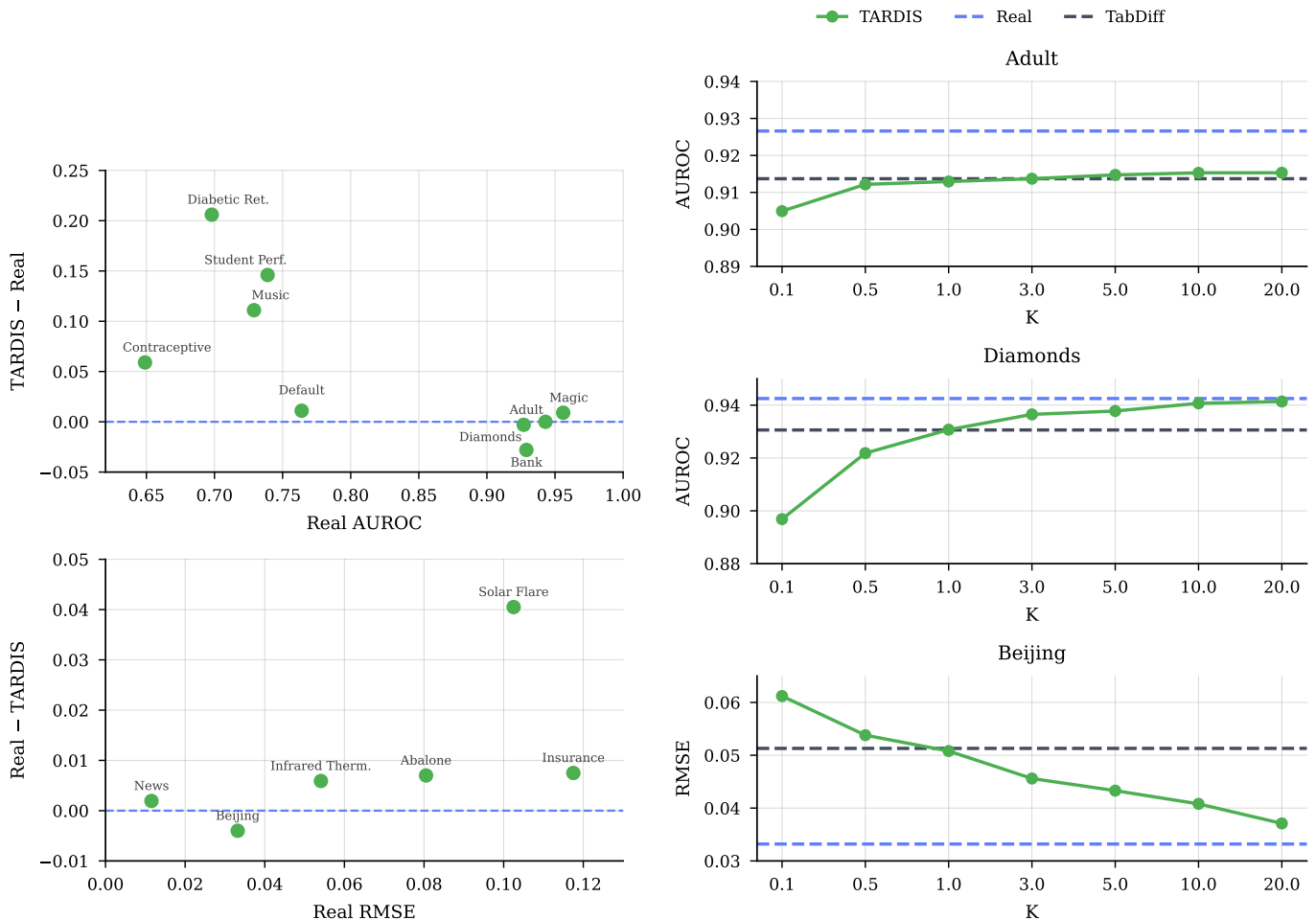
Table 2: Fidelity, diversity, and privacy proxies across 15 datasets.

Metric	TabDiff	TARDIS
Precision \uparrow	0.947 \pm 0.073	0.949\pm0.069
Recall \uparrow	0.994 \pm 0.005	0.995\pm0.005
DCR-1 share	0.501\pm0.010	0.499\pm0.013
NNDR \uparrow	0.823 \pm 0.115	0.824\pm0.107

utility-aware curation.

Privacy. DCR-1 share and NNDR are likewise preserved at the backbone level (Table 2; per-dataset breakdown in Table 8): TARDIS DCR-1 share 0.499 ± 0.013 vs. TabDiff 0.501 ± 0.010 , NNDR 0.824 ± 0.107 vs. 0.823 ± 0.115 , with no per-dataset deviation exceeding 0.04. TARDIS does not improve privacy (which is not a claim of this paper) and the post-hoc selection mechanism does not degrade it either: although the Chamfer Sampler ranks candidates by proximity to a real reference batch, the bidirectional structure of \mathcal{C} balances fidelity against coverage, preventing convergence onto training records.

Runtime. On the Nvidia GTX 1080 Ti, TARDIS adds 0.9 to 79.4 minutes of wall-clock time on top of the trained backbone, with a median of 16.1 minutes across the 15 datasets; the largest case (Bank, $\sim 45,000$ instances) runs in 79.4 minutes and the smallest (Solar Flare) in 0.9 minutes (per-stage breakdown in Appendix H). Stage II



(a) Per-dataset $\Delta\%$ over $\mathcal{U}_{\text{real}}$ as a function of the real-data baseline, classification (top, AUROC) and regression (bottom, RMSE). Gains concentrate on datasets with low $\mathcal{U}_{\text{real}}$.

(b) Cardinality saturation: sweep of K with $M = 50$ on Adult, Diamonds, and Beijing, the three benchmarks where TARDIS yields the smallest gain over Real (Table 1). TARDIS still overtakes TabDiff near $K \approx 1.0$ on all three.

Figure 2: Empirical signatures of TARDIS performance: utility headroom (left) and cardinality saturation (right).

generation accounts for 47% to 90% of the wall-clock budget; Stage III selection contributes 5% to 38%, with the highest fractions on Music and News (both 38%) where the candidate pool is large; GKD distillation contributes 7% to 11% on the two datasets where it is active. The dominant cost factor is the $M = 50$ oversampling, which is GPU-throughput-bound and shrinks proportionally on modern hardware.

5 Discussion and Limitations

BCR as a domain-transferable principle. The Chamfer functional of Equation 3 is modality-agnostic: it requires only a differentiable representation map φ and a real-data reference batch. Its two operationalizations (continuous via $\nabla_{x_t} \mathcal{C}$ during reverse diffusion, discrete via batch ranking after sampling) extend to image, text, and joint multimodal diffusion under domain-appropriate encoders, since neither a differentiable score nor a candidate pool is tabular-specific. The configuration-level signature of Section 4.2, with the unconstrained search electing the joint guided-and-Chamfer regime in 9 of 15 cases, is the empirical claim BCR makes about its generality. Two fur-

ther findings sharpen this picture. First, the TARDIS \times 1 ablation (Section 4.1) isolates Stage II from Stage III: continuous guidance alone yields mean +1.4% over TabDiff but does not surpass real-data utility, while the full pipeline with bidirectional discrete selection does. The discrete level thus carries the dominant share of the gap-closing effect, inverting the image-domain emphasis on score-level guidance. Second, sample-level privacy is preserved as a structural property of the bidirectional functional: the coverage term penalizes distributional collapse onto D_{real} , so ranking by proximity at Stage III cannot drive synthetic samples onto training records (Section 4.3). Refinement is therefore complementary to backbone improvement, not a substitute: any competent tabular diffusion backbone admits this inference-time refinement at fixed compute overhead, with gains concentrated on the regimes where synthetic data is most operationally needed (small corpora, label noise, class imbalance).

Limitations and Future Work. TARDIS is empirically validated on a single backbone (TabDiff); BCR is backbone-agnostic by construction, but transfer to TabSyn (latent-space diffusion) and TabDDPM (multinomial diffusion) is not empirically tested, and Stage II’s score perturba-

tion does not apply to autoregressive (TabularARGN) or variational (TVAE) decoders. The oversampling factor M is fixed at 50, leaving the M -dependence of the saturation knee uncharacterized. The headline configurations use deterministic samplers, so per-seed variance reflects pool generation only, and downstream-learner transfer beyond XGBoost is not tested. Privacy is reported through DCR-1 and NNDR proxies, without formal differential-privacy claims or membership-inference evaluation. Future work targets three directions: cross-backbone and cross-modality transfer (TabSyn, TabD-DPM, image-domain diffusion); an M -sweep enabling an adaptive recipe driven by N_r , manifold-coverage gap, and deployment cardinality budget; and a differentially-private variant consuming calibrated budget at both refinement levels.

6 Conclusions

We introduced TARDIS, an inference-time refinement framework for pre-trained tabular diffusion backbones, grounded in the *Bidirectional Chamfer Refinement* (BCR) principle: a single Chamfer functional minimized continuously during reverse diffusion via score-level guidance and discretely after sampling via batch ranking, with the per-dataset search recovering this joint structure on 9 of 15 benchmarks and selecting single-stage variants on the remaining 6. Across 15 heterogeneous tabular benchmarks (binary, multiclass, regression), TARDIS achieves a median +8.6% improvement in ψ over models trained on real data (Wilcoxon $p = 0.016$, 11/15 strict wins) and improves over the TabDiff backbone on every dataset (mean +12.9%, $p < 10^{-4}$), with fidelity, diversity, and privacy preserved at the backbone level and a wall-clock overhead under 80 minutes on a 2017 consumer GPU. The synthetic–real gap is therefore not primarily a training-time problem on the studied corpus, and BCR provides a domain-transferable principle for inference-time refinement of pre-trained generative models.

References

- [1] James Bergstra, Daniel Yamins, and David Cox. Making a science of model search: Hyperparameter optimization in hundreds of dimensions for vision architectures. In *International conference on machine learning*, pages 115–123. PMLR, 2013.
- [2] Christopher P Burgess, Irina Higgins, Arka Pal, Loic Matthey, Nick Watters, Guillaume Desjardins, and Alexander Lerchner. Understanding disentangling in beta-vae. *arXiv preprint arXiv:1804.03599*, 2018.
- [3] Ricardo JGB Campello, Davoud Moulavi, and Jörg Sander. Density-based clustering based on hierarchical density estimates. In *Pacific-Asia Conference on Knowledge Discovery and Data Mining*, 2013.
- [4] Nitesh V Chawla, Kevin W Bowyer, Lawrence O Hall, and W Philip Kegelmeyer. Smote: synthetic minority over-sampling technique. *Journal of artificial intelligence research*, 16:321–357, 2002.
- [5] Tianqi Chen and Carlos Guestrin. Xgboost: A scalable tree boosting system. In *Proceedings of the 22nd acm sigkdd international conference on knowledge discovery and data mining*, pages 785–794, 2016.
- [6] Nicola Dall’Asen, Xiaofeng Zhang, Reyhane Askari Hemmat, Melissa Hall, Jakob Verbeek, Adriana Romero-Soriano, and Michal Drozdal. Increasing the utility of synthetic images through chamfer guidance. *arXiv preprint arXiv:2508.10631*, 2025.
- [7] Maria F Davila R, Sven Groen, Fabian Panse, and Wolfram Wingerath. Navigating tabular data synthesis research understanding user needs and tool capabilities. *ACM SIGMOD Record*, 53(4):18–35, 2025.
- [8] Daniel G"arber and Lea Demelius. Iterative subset selection for high-fidelity synthetic tabular data. In *EurIPS 2025 Workshop: AI for Tabular Data*, 2025.
- [9] EU GDPR. General data protection regulation (gdpr). *Cit. on*, page 4, 2018.
- [10] Geoffrey Hinton, Oriol Vinyals, and Jeff Dean. Distilling the knowledge in a neural network. *arXiv preprint arXiv:1503.02531*, 2015.
- [11] Jonathan Ho and Tim Salimans. Classifier-free diffusion guidance. *arXiv preprint arXiv:2207.12598*, 2022.
- [12] Jonathan Ho, Ajay Jain, and Pieter Abbeel. Denoising diffusion probabilistic models. *Advances in neural information processing systems*, 33:6840–6851, 2020.
- [13] Jayoung Kim, Chaejeong Lee, and Noseong Park. Stasy: Score-based tabular data synthesis. *arXiv preprint arXiv:2210.04018*, 2022.
- [14] Diederik P Kingma and Max Welling. Auto-encoding variational bayes. *arXiv preprint arXiv:1312.6114*, 2013.
- [15] Akim Kotelnikov, Dmitry Baranchuk, Ivan Rubachev, and Artem Babenko. Tabddpm: Modelling tabular data with diffusion models. In *International conference on machine learning*, pages 17564–17579. PMLR, 2023.
- [16] Tuomas Kynkäänniemi, Tero Karras, Samuli Laine, Jaakko Lehtinen, and Timo Aila. Improved precision and recall metric for assessing generative models. *Advances in neural information processing systems*, 32, 2019.
- [17] Chaejeong Lee, Jayoung Kim, and Noseong Park. Codi: Co-evolving contrastive diffusion models for mixed-type tabular synthesis. In *International Conference on Machine Learning*, pages 18940–18956. PMLR, 2023.
- [18] Eugenio Lomurno and Matteo Matteucci. Federated knowledge recycling: Privacy-preserving synthetic data sharing. *Pattern Recognition Letters*, 190:124–130, 2025.

- [19] Eugenio Lomurno and Matteo Matteucci. Synthetic image learning: Preserving performance and preventing membership inference attacks. *Pattern Recognition Letters*, 190:52–58, 2025.
- [20] Juntong Shi, Minkai Xu, Harper Hua, Hengrui Zhang, Stefano Ermon, and Jure Leskovec. Tabdiff: a mixed-type diffusion model for tabular data generation. *arXiv preprint arXiv:2410.20626*, 2024.
- [21] Andrey Sidorenko, Ivona Krchova, Mariana Vargas Vieyra, Paul Tiwald, Mario Scriminaci, and Michael Platzer. Tabularargn: An auto-regressive generative network for tabular data generation. In *EurIPS 2025 Workshop: AI for Tabular Data*, 2025.
- [22] Mihaela CĂ Stoian, Eleonora Giunchiglia, and Thomas Lukasiewicz. A survey on tabular data generation: Utility, alignment, fidelity, privacy, and beyond. *arXiv preprint arXiv:2503.05954*, 2025.
- [23] HaiYing Wang, Min Yang, and John Stufken. Information-based optimal subdata selection for big data linear regression. *Journal of the American Statistical Association*, 114(525):393–405, 2019.
- [24] Lei Xu, Maria Skoularidou, Alfredo Cuesta-Infante, and Kalyan Veeramachaneni. Modeling tabular data using conditional gan. *Advances in neural information processing systems*, 32, 2019.
- [25] Hengrui Zhang, Jiani Zhang, Balasubramaniam Srinivasan, Zhengyuan Shen, Xiao Qin, Christos Faloutsos, Huzefa Rangwala, and George Karypis. Mixed-type tabular data synthesis with score-based diffusion in latent space. *arXiv preprint arXiv:2310.09656*, 2023.
- [26] Zilong Zhao, Aditya Kunar, Robert Birke, Hiek Van der Scheer, and Lydia Y Chen. Ctab-gan+: Enhancing tabular data synthesis. *Frontiers in big Data*, 6:1296508, 2024.

A Bidirectional Chamfer Refinement: Properties and Saturation

This appendix collects the structural properties of the symmetric Chamfer functional \mathcal{C} (Section A.1), the saturation argument that motivates the empirical knee structure of Figure 2b (Section A.2), and its empirical validation on the cardinality sweep of Section 4.2 (Section A.3).

A.1 Properties of the Symmetric Chamfer Functional

Let $\varphi : \mathcal{X} \rightarrow \mathbb{R}^d$ be a representation map and $A, B \subset \mathcal{X}$ finite multisets with φ injective on $A \cup B$. The functional \mathcal{C} of Equation 3 satisfies: **(P1) non-negativity**, $\mathcal{C}(A, B) \geq 0$ (Euclidean norm under uniform weighting); **(P2) identity of indiscernibles**, $\mathcal{C}(A, B) = 0 \iff \varphi(A) = \varphi(B)$ as multisets, since fidelity and coverage terms vanish jointly only when the two sets coincide in φ -space; **(P3) symmetry**, $\mathcal{C}(A, B) = \mathcal{C}(B, A)$ by construction. P1–P3 jointly justify the use of \mathcal{C} as a single optimization target: minimizing $\mathcal{C}(D_{\text{syn}}, D_{\text{real}})$ at the continuous (Stage II) and discrete (Stage III) refinement levels is a coherent objective, since any reduction at one level corresponds to monotone movement toward the same target distribution in φ -space.

A.2 The BCR Saturation Argument

We argue that, under reasonable assumptions on the candidate pool and the discrete sampler, \mathcal{U}_{syn} exhibits a monotone-then-plateau dependence on the subsampling fraction K , with the knee location governed by the M/K ratio. We state this as a principled argument rather than a formal theorem: we do not characterize the convergence rate as $M \rightarrow \infty$, the empirical knee depends on the intrinsic dimension of D_{real} in φ -space which we do not formalize, and we hold $M = 50$ fixed throughout our experiments.

Argument (BCR Saturation). Under the assumptions that (i) Stage II concentrates the empirical density of $\varphi(D_{\text{cand}})$ around the support of $\varphi(D_{\text{real}})$, (ii) Stage III selects the top K/M fraction of D_{cand} by \mathcal{C} -rank, and (iii) the downstream learner is consistent in the cardinality of training data, we expect \mathcal{U}_{syn} to be monotonically non-decreasing in M/K and to saturate at $K = K^*$ for a dataset-dependent knee $K^* \leq M$.

Reasoning. As K decreases relative to M , the Stage III sampler retains only the most \mathcal{C} -aligned candidates, sharpening $\varphi(D_{\text{syn}})$ around the support of $\varphi(D_{\text{real}})$ and reducing the fidelity term m_{sr} of Equation 6; as $K \rightarrow M$, the selection becomes vacuous and the discrete refinement contributes negligibly. Saturation occurs when the coverage term m_{rs} becomes the binding constraint, i.e., when a smaller selection fraction risks under-covering isolated regions of the real-data manifold. The knee K^* is expected to scale with the effective intrinsic dimension of D_{real} in φ -space and with the inverse local density of real samples.

A.3 Empirical Validation

The cardinality sweep $K \in \{0.1, 0.5, 1, 3, 5, 10, 20\}$ with $M = 50$ on Adult, Diamonds, and Beijing (Figure 2b) verifies the predicted monotone-then-plateau profile. The knees occur at $K^* \approx 3$ for Adult, $K^* \approx 5$ for Diamonds, and beyond $K = 20$ for Beijing, an ordering consistent with the intrinsic-dimension intuition (Adult mixed-type but compact; Beijing combines hourly cycles and multi-scale meteorology, yielding the highest effective dimension).

B Backbone Selection

The choice of TabDiff [20] as the underlying backbone for TARDIS results from a controlled head-to-head comparison against TabSyn [25] and TabularARGN [21] on 10 of the 15 corpus benchmarks (Adult, Default, Magic, Bank, Music, Diamonds, Abalone, Insurance, Beijing, News), for which all three baselines have been independently trained at matched 1:1 cardinality. Each backbone was evaluated under the same TSTR protocol of Section 4, with multiple utility and fidelity metrics per dataset.

Aggregate dominance. Of the 50 metric cells, TabDiff dominates on 23, TabSyn on 14, and TabularARGN on 13, with dominance concentrated on the primary TSTR metrics (classification AUROC, regression RMSE). TabularARGN remains competitive on Bank classification, where its autoregressive factorization handles class-conditional distributions effectively, and on News regression, where the high-dimensional feature space (46 attributes) favors per-feature autoregressive heads over latent-space diffusion.

Architecture and TARDIS compatibility. TabDiff’s per-feature noise schedules differentiate noising rates across features of heterogeneous scale and cardinality, avoiding the bias that a single shared schedule introduces on mixed-type inputs; its continuous reverse process and exposed score ε_θ make it directly compatible with the Stage II score perturbation of Equation 5. TabSyn is similarly compatible via latent-space score perturbation, but loses the per-feature inductive bias. TabularARGN and variational generators (e.g., TVAE) are excluded from Stage II since the perturbation presumes a continuous reverse process; Stage III remains compatible with any generator producing a candidate pool, so the discrete level of BCR transfers to those generators independently.

Table 3: Backbone comparison on 10 corpus benchmarks under matched 1:1 cardinality. Primary downstream metric reported: AUROC \uparrow for binary classification, weighted-AUROC \uparrow for multiclass classification, RMSE \downarrow for regression. Bold indicates the best generator per column, excluding Real. The final column reports the average percentage delta with respect to Real, computed as $100(m - r)/r$ for AUROC and $100(r - m)/r$ for RMSE; higher is better.

Model	Classification (AUROC \uparrow)						Regression (RMSE \downarrow)				$\Delta\%$ vs Real \uparrow
	Adult	Default	Magic	Bank	Music	Diamonds	Abalone	Insurance	Beijing	News	Avg.
Real	.927	.764	.956	.929	.729	.943	.081	.118	.033	.01154	–
TabularARGN	.914	.751	.909	.911	.714	.907	.096	.281	.062	.01117	–25.72
TabSyn	.908	.768	.942	.896	.724	.929	.079	.132	.055	.01201	–8.88
TabDiff	.913	.765	.940	.856	.823	.930	.079	.132	.051	.01194	–6.68

C Stage II Schedules and Reference Batching

This appendix specifies the schedule families exposed to the TPE search: the guidance scaling $\Gamma(t)$ of Stage II (Section C.1), the KL annealing weight $\beta(t)$ used during β -VAE training of φ (Section C.2), and the reference batching strategies (Section C.3). Bounds $\gamma_{\min}/\gamma_{\max}$ and $\beta_{\min}/\beta_{\max}$ are selected per dataset.

C.1 Guidance Schedules $\Gamma(t)$

Let T denote the total number of reverse-diffusion steps, with $t \in [0, T]$ counting from $t = T$ (pure noise) to $t = 0$ (final sample). We define four functional families for $\Gamma(t)$, each parameterized by $(\gamma_{\min}, \gamma_{\max})$ and bounded in $[\gamma_{\min}, \gamma_{\max}]$:

$$\text{Constant: } \Gamma(t) = \gamma_{\max} \quad (7)$$

$$\text{Linear: } \Gamma(t) = \gamma_{\min} + (\gamma_{\max} - \gamma_{\min}) \cdot \frac{t}{T} \quad (8)$$

$$\text{Cosine: } \Gamma(t) = \gamma_{\min} + \frac{1}{2}(\gamma_{\max} - \gamma_{\min}) (1 + \cos(\pi \cdot \frac{t}{T})) \quad (9)$$

$$\text{Sine: } \Gamma(t) = \gamma_{\max} - \frac{1}{2}(\gamma_{\max} - \gamma_{\min}) (1 + \cos(\pi \cdot \frac{t}{T})) \quad (10)$$

Behavioral characterization. Constant applies uniform guidance across the trajectory. Linear and Sine rise monotonically from γ_{\min} at $t = 0$ to γ_{\max} at $t = T$ (Sine with cosine curvature, Linear straight); Cosine is the mirror image, decaying monotonically from γ_{\max} at $t = 0$ to γ_{\min} at $t = T$.

C.2 KL Annealing Schedules $\beta(t)$

Let T_{VAE} denote the total number of training epochs of the β -VAE encoder φ . We define five functional families for the KL weight $\beta(t)$, each parameterized by $(\beta_{\min}, \beta_{\max})$:

$$\text{Constant: } \beta(t) = \beta_{\max} \quad (11)$$

$$\text{Linear: } \beta(t) = \beta_{\max} \cdot \min\left(1, \frac{t}{T_{\text{VAE}}}\right) \quad (12)$$

$$\text{Cosine: } \beta(t) = \beta_{\min} + \frac{1}{2}(\beta_{\max} - \beta_{\min}) \left(1 + \cos\left(\pi \frac{t}{T_{\text{VAE}}}\right)\right) \quad (13)$$

$$\text{Sine: } \beta(t) = \beta_{\max} - \frac{1}{2}(\beta_{\max} - \beta_{\min}) \left(1 + \cos\left(\pi \frac{t}{T_{\text{VAE}}}\right)\right) \quad (14)$$

$$\text{Cyclical: } \beta(t) = \beta_{\max} \cdot \frac{t \bmod T_{\text{cyc}}}{T_{\text{cyc}}} \quad (15)$$

Linear and Sine implement standard KL warmup (low β early, β_{\max} at convergence); Cosine inverts the profile, decaying from β_{\max} at initialization to β_{\min} . The Cyclical schedule alternates between regularized and reconstruction-emphasized regimes to mitigate posterior collapse on high-cardinality categorical features.

C.3 Reference Batching

The reference batch x_r used in Equation 5 is sampled at the start of each generation and held fixed across all reverse-diffusion steps. Two batching strategies are exposed to the TPE search:

Class-conditional batching. For classification tasks, x_r is drawn from the same target class as the candidate batch x_t . This concentrates the gradient $\nabla_{x_t} \mathcal{C}$ on the conditional manifold relevant to the candidate’s target class.

Global batching. x_r is drawn uniformly from D_{real} . It is the default for regression, where there is no class structure, and is exposed as an alternative for classification tasks where class-conditional sampling under-represents the global manifold structure.

Per-dataset selection is reported in Appendix F, Table 6.

D Stage III Sampler Definitions

This appendix defines the five sampler variants composing the Stage III grid: the Chamfer Sampler (Section D.1, recap from main text), and the four alternatives Stratified, IBOSS, HDBSCAN, and MDSampler (Sections D.2–D.5). All samplers operate on the candidate pool D_{cand} of cardinality $M \cdot N_r$ produced by Stage II and return a subset of cardinality $K \cdot N_r$ that constitutes the synthetic dataset D_{syn} .

D.1 Chamfer Sampler

The Chamfer Sampler (Section 3.3) partitions D_{cand} into batches $\{B_k\}$ of size b , ranks each by $\mathcal{C}(B_k, D_{\text{real}})$ (Equation 6), and retains the union of the top-ranked batches up to $K \cdot N_r$ samples. It is the discrete counterpart of Stage II’s score perturbation, both minimizing \mathcal{C} in φ -space.

D.2 Stratified Sampler

The Stratified Sampler partitions D_{cand} along the target variable for classification tasks, or along quantile bins of the target for regression, and samples uniformly within each stratum to match the per-class frequencies of D_{real} . The selection is independent of feature-space proximity, retaining only the marginal target distribution of the real set.

D.3 IBOSS Sampler

IBOSS (Information-Based Optimal Subdata Selection) [23] selects candidates that span the feature space, ensuring every region of the candidate manifold has comparable representation in D_{syn} . It favors extremal points at the boundary of the candidate distribution and is target-agnostic, operating independently of D_{real} .

D.4 HDBSCAN Sampler

The HDBSCAN Sampler clusters D_{cand} in φ -space using the HDBSCAN algorithm [3] with `min_cluster_size = b`, retaining the top $K \cdot N_r$ clusters by density. It exploits the manifold structure of the candidate pool but is one-directional with respect to the real-data manifold: synthetic-pool clusters are selected without aligning to D_{real} .

D.5 MDSampler

The MDSampler (Manifold-Distance Sampler) approximates the support of $\varphi(D_{\text{real}})$ as the union of k -nearest-neighbor *hyperspheres* around each real point in φ -space, with each *hypersphere* centered at $\varphi(r)$ and radius $\rho_k(r)$ equal to the distance from $\varphi(r)$ to its k -th nearest neighbor in $\varphi(D_{\text{real}})$ (we use $k = 10$). Each candidate $x \in D_{\text{cand}}$ is scored by its distance to this estimated manifold,

$$d_{\text{MD}}(x) = \min_{r \in D_{\text{real}}} \max(0, \|\varphi(x) - \varphi(r)\|_2 - \rho_k(r)), \quad (16)$$

which is zero whenever x lies inside any *hypersphere* and equals the distance from the nearest *hypersphere* boundary otherwise. The MDSampler retains the $K \cdot N_r$ candidates with smallest d_{MD} , prioritizing candidates inside the real-data manifold and falling back on the closest off-manifold ones once the inside set is exhausted. The construction follows the manifold Precision proxy of [16]: $d_{\text{MD}} = 0$ corresponds to the inside-the-manifold criterion that defines that metric. The MDSampler is the fidelity-driven counterpart of the bidirectional Chamfer Sampler: when Stage II is disabled, the candidate pool retains broad coverage by construction, the coverage term m_{rs} of Equation 6 is approximately satisfied a priori, and inside-manifold selection suffices; when Stage II is enabled and concentrates the pool around $\varphi(D_{\text{real}})$, most candidates already satisfy $d_{\text{MD}} \approx 0$ and the bidirectional Chamfer Sampler is needed to discriminate via coverage.

E Generative Knowledge Distillation Details

This appendix details the Generative Knowledge Distillation (GKD) component of Stage III, introduced in Section 3.3.

Procedure. GKD trains a teacher classifier $f_{\text{GKD}} : \mathcal{X} \rightarrow \Delta^{|\mathcal{Y}|-1}$ on D_{real} , where $\Delta^{|\mathcal{Y}|-1}$ denotes the $(|\mathcal{Y}| - 1)$ -dimensional probability simplex. For each candidate $\hat{x}_j \in D_{\text{cand}}$ produced by Stage II, the hard target \hat{y}_j is replaced by

the soft-label distribution $f_{\text{GKD}}(\hat{x}_j)$, yielding the relabeled set

$$D_{\text{cand}}^{\text{GKD}} = \{(\hat{x}_j, f_{\text{GKD}}(\hat{x}_j))\}_{j=1}^{|D_{\text{cand}}|}, \quad (17)$$

which is then passed to Stage III’s sampler in place of D_{cand} . The downstream learner A trains under cross-entropy with soft targets. GKD relabels targets only, leaving feature vectors \hat{x}_j unchanged.

Teacher classifier. In our experiments f_{GKD} is XGBoost trained on D_{real} under the same hyperparameter search as the downstream learner A , with predicted-probability outputs used as soft labels. Matching f_{GKD} to the architectural family of A reduces teacher-student mismatch.

Restriction to classification. GKD is structurally undefined for continuous regression targets: soft labels over \mathbb{R} require a parametric assumption (e.g., Gaussian conditional) unrelated to the BCR mechanism. GKD is therefore disabled by construction on the 6 regression datasets, halving the Stage III grid on those.

Selection regime. The empirical regime in which GKD is selected is characterized in Section 4.2 (Low-cardinality regime).

F Per-Dataset Configurations

This appendix reports the per-dataset structural attributes of the 15 corpus benchmarks (Section F.1, Table 4), the search space optimized by the Tree-structured Parzen Estimator over Stage II hyperparameters (Section F.2, Table 5), and the configuration retained per dataset against the validation split (Section F.3, Table 6).

F.1 Dataset Summary

Table 4 reports the structural attributes of the 15 corpus benchmarks, sourced from UCI and Kaggle. Three datasets contain missing values (Adult, Beijing, Infrared Thermography), imputed identically across all models: median for numerical features, mode for categorical, per training split.

Table 4: Dataset summary. n = number of instances; d = number of feature columns excluding the target; d_n/d_c = numerical / categorical feature counts; NaN indicates presence of missing values (imputed identically across all models, see Appendix F).

Dataset	Task	n	d	d_n	d_c	NaN
<i>Binary classification</i>						
Adult	BC	48,842	14	6	8	Yes
Bank	BC	45,211	16	7	9	No
Default	BC	30,000	23	14	9	No
Diabetic Retinopathy	BC	1,151	19	19	0	No
Magic	BC	19,020	10	10	0	No
<i>Multiclass classification</i>						
Contraceptive	MC (3)	1,473	9	2	7	No
Diamonds	MC (5)	53,940	9	6	3	No
Music	MC (11)	25,709	14	13	1	No
Student Performance	MC (4)	666	11	0	11	No
<i>Regression</i>						
Abalone	R	4,177	8	7	1	No
Beijing	R	43,824	11	6	5	Yes
Infrared Thermography	R	1,020	33	30	3	Yes
Insurance	R	987	10	3	7	No
News	R	39,644	46	44	2	No
Solar Flare	R	1,066	10	7	3	No

F.2 TPE Search Space

Table 5 reports the Stage II hyperparameter search space optimized per dataset by the Tree-structured Parzen Estimator. The β -VAE inner study (latent dimension and KL annealing schedule) is invoked only when the outer search selects β -VAE mapping; its functional families are reported in Appendix C.2.

F.3 Selected Per-Dataset Configurations

Table 6 reports the configuration retained per dataset by the search procedure against the validation split.

Table 5: Stage II hyperparameter search space optimized per dataset by the Tree-structured Parzen Estimator. Domains follow Optuna conventions: *Cat* = categorical, *Int* = integer-valued with the indicated step, *Log* = log-uniform, *Lin* = linear with the indicated step. The β -VAE inner study (latent dimension and KL annealing schedule) is invoked only when the outer search selects β -VAE mapping; its search space is reported in Appendix C.

Parameter	Domain	Description	Scale
K	[0.1, 25.0]	Final cardinality multiplier	Lin (0.1)
Guidance variant	{None, identity, β -VAE}	Toggle and form of φ	Cat
Schedule $\Gamma(t)$	{constant, linear, cosine, sine}	Guidance scaling family	Cat
γ_{\max}	$[10^{-1}, 5.0]$	Upper bound of $\Gamma(t)$	Log
γ_{\min}	$[10^{-8}, \gamma_{\max} - 0.1]$	Lower bound of $\Gamma(t)$	Log
t_g	[3, 20]	Guidance step count	Int (1)
Batching ratio	{None, 1, 1/2, 1/4, 1/8, 1/10}	Class-conditional fraction	Cat

Table 6: Per-dataset configurations selected by the search procedure against the validation split. Stage II hyperparameters from TPE optimization; Stage III combination from grid search over {GKD off, GKD on} \times {Stratified, IBOSS, HDBSCAN, MDSampler, Chamfer Sampler}. Columns: K cardinality multiplier; G guidance toggle (\times disabled, \checkmark enabled); Γ schedule family (Section C.1); φ representation map (β -VAE(d) for β -VAE mapping with latent dimension d , identity for identity mapping, dash when guidance is disabled); B_{ratio} reference batching fraction; Type class-conditional (*cls*) or global (*glob*). CS = Chamfer Sampler, MD = MDSampler.

Dataset	Stage II (TPE)						Stage III (grid)	
	K	G	Γ	φ	B_{ratio}	Type	GKD	Sampler
Adult	0.5	\times	–	–	–	cls	\checkmark	CS
Bank	24.9	\times	–	–	–	cls	\times	MD
Default	13.1	\checkmark	cosine	identity	1/4	cls	\times	CS
Diabetic Retin.	22.5	\checkmark	cosine	β -VAE(4)	1/2	cls	\times	CS
Magic	23.9	\times	–	–	–	cls	\times	MD
Contraceptive	8.5	\checkmark	sine	β -VAE(16)	1/4	cls	\times	CS
Diamonds	23.1	\checkmark	sine	β -VAE(4)	1/4	cls	\times	CS
Music	20.0	\times	–	–	–	cls	\times	MD
Student Perf.	15.2	\checkmark	cosine	β -VAE(16)	1/8	cls	\times	CS
Abalone	23.0	\times	–	–	–	glob	\times	MD
Beijing	20.0	\checkmark	cosine	identity	1	glob	\times	CS
Infrared Therm.	12.8	\checkmark	cosine	β -VAE(32)	1/2	glob	\times	CS
Insurance	10.0	\checkmark	sine	identity	1/10	glob	\times	CS
News	14.8	\checkmark	constant	β -VAE(4)	1/8	glob	\times	CS
Solar Flare	0.1	\times	–	–	–	glob	\checkmark	CS

Aggregate selection counts. The configuration space partitions cleanly along the Stage II guidance toggle. Of the 9 datasets enabling guidance, 3 select identity mapping in the data space (Default, Beijing, Insurance) and 6 select β -VAE mapping in the encoder’s latent space (Diabetic Retinopathy, Contraceptive, Diamonds, Student Performance, Infrared Thermography, News); all 9 select the Chamfer Sampler in Stage III. Of the 6 datasets disabling guidance, 4 select the MDSampler (Bank, Magic, Music, Abalone) and 2 select the Chamfer Sampler with GKD enabled (Adult $K=0.5$, Solar Flare $K=0.1$, both within the low-cardinality regime $K \leq 1$). GKD is therefore selected on 2 of 15 datasets, both classification datasets at low K . Reference batching is class-conditional on all 9 classification datasets and global on all 6 regression datasets, consistent with the structural distinction between the two task families.

G Auxiliary Metrics

This appendix reports auxiliary metrics complementing the AUROC, weighted-AUROC, and RMSE numbers of Table 1: F1 for classification benchmarks (Section G.1) and per-dataset DCR-1 share and NNDR breakdowns (Section G.2). The fidelity (Precision) and diversity (Recall) numbers are reported aggregated in Table 2 of the main text.

G.1 Classification F1

F1 dominance. TARDIS achieves the best F1 on 8 of 9 classification datasets, with the only exception on Adult (0.707 Real vs. 0.704 TARDIS). Gains concentrate on datasets with strong class imbalance or low-cardinality minority classes (Diabetic Retinopathy, Student Performance, Bank), consistent with BCR retaining samples aligned with real-data class-conditional manifolds.

Table 7: Per-dataset auxiliary downstream classification metrics under TSTR: F1 for binary classification, macro-F1 for multiclass classification. Best per row in bold.

Dataset	Metric	Real	TabDiff	TARDIS \times 1	TARDIS
Diabetic Retin.	F1	0.5329	0.5469	0.5999	0.7407
Adult	F1	0.707	0.671	0.696	0.704
Default	F1	0.447	0.443	0.460	0.460
Magic	F1	0.862	0.817	0.837	0.880
Bank	F1	0.538	0.463	0.503	0.562
Student Perf.	macro-F1	0.5076	0.5119	0.3972	0.7299
Contraceptive	macro-F1	0.4229	0.4622	0.4671	0.5322
Music	macro-F1	0.364	0.470	0.471	0.489
Diamonds	macro-F1	0.801	0.774	0.787	0.804

G.2 Per-Dataset Privacy Breakdown

Table 8: Per-dataset DCR-1 share (closer to 0.50 indicates better balance between train-data proximity and novelty) and NNDR (higher indicates more diverse synthetic samples).

Dataset	DCR-1 share		NNDR	
	TabDiff	TARDIS	TabDiff	TARDIS
Solar Flare	0.4906	0.5063	0.8876	0.8673
Infrared Therm.	0.5283	0.4902	0.9517	0.9540
Abalone	0.490	0.494	0.853	0.852
Insurance	0.487	0.487	0.762	0.773
Beijing	0.501	0.500	0.857	0.857
News	0.503	0.505	0.942	0.943
Diabetic Retin.	0.5068	0.5382	0.8706	0.8689
Adult	0.502	0.498	0.769	0.768
Default	0.505	0.500	0.822	0.823
Magic	0.501	0.491	0.882	0.879
Bank	0.489	0.497	0.911	0.910
Student Perf.	0.5008	0.4758	0.4970	0.5373
Contraceptive	0.5061	0.5023	0.6995	0.6871
Music	0.506	0.504	0.883	0.877
Diamonds	0.500	0.499	0.761	0.761

Privacy preservation. TARDIS DCR-1 share remains within ± 0.04 of TabDiff on all 15 datasets, with most absolute deviations under ± 0.02 . The three largest deviations (Infrared Thermography -0.0381 , Diabetic Retinopathy $+0.0314$, Student Performance -0.0250) correspond to small-corpus datasets where DCR-1 is more sensitive to the specific subset retained by Stage III. NNDR is similarly preserved; the largest deviation on Student Performance ($+0.0403$) reflects an unusually low TabDiff baseline (0.4970) on a 666-instance dataset where the metric is unstable.

H Runtime Breakdown

This appendix details the per-dataset wall-clock time of the TARDIS refinement pipeline (Nvidia GTX 1080 Ti, 12 GB, 2017 consumer GPU). Per-stage runtimes are reported in Table 9 and visualized in Figure 3. Total times include only the TARDIS refinement passes; TabDiff backbone training is performed once per dataset and reused across configurations.

Table 9: Per-dataset TARDIS runtime breakdown. Stage II is the guided generation of D_{cand} ($M = 50$); Stage III is the post-hoc selection (Chamfer Sampler or MDSampler); GKD is the soft-label distillation overhead, applicable only when the configuration enables it. Datasets sorted by total runtime ascending.

Dataset	Stage II (min)	Stage III (min)	GKD (min)	Total (min)
Solar Flare	0.7	0.1	0.1	0.9
Insurance	0.8	0.2	–	1.1
Student Perf.	1.0	0.2	–	1.4
Diabetic Retin.	1.2	0.3	–	1.7
Contraceptive	1.8	0.1	–	2.0
Infrared Therm.	1.3	0.6	–	2.1
Abalone	2.5	1.0	–	3.8
Magic	9.8	4.9	–	16.1
Music	14.3	11.4	–	29.8
Adult	22.9	7.0	2.3	32.2
Default	38.5	7.1	–	47.9
Beijing	45.3	4.9	–	53.7
Diamonds	43.3	16.0	–	65.3
News	36.3	29.8	–	77.7
Bank	65.7	10.1	–	79.4

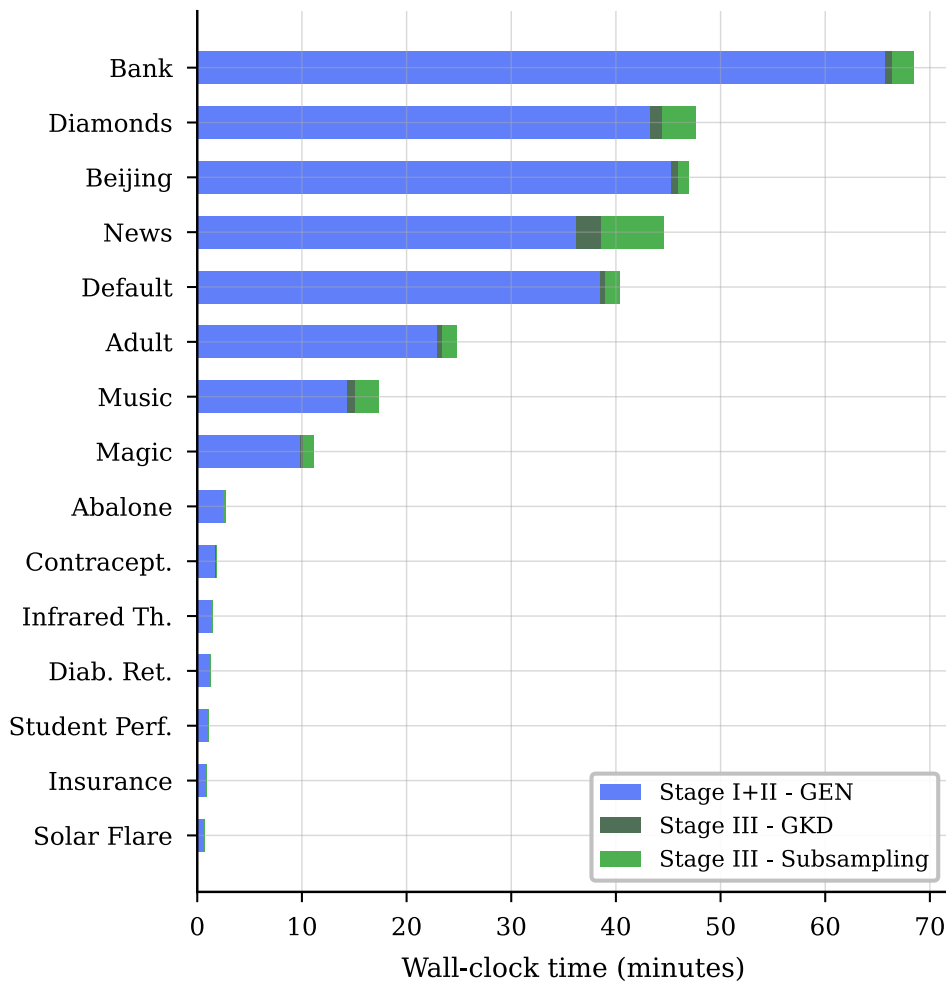


Figure 3: Stacked-bar visualization of Table 9, with stages ordered Stage II (guided generation), Stage III (selection), GKD. Datasets sorted by total runtime ascending.